

APPLIED RESEARCH

Decoupled Unipolar Hysteresis Current Control for Single-Phase Grid-Tied Inverter Without Current Zero-Crossing Distortion

RUI XIE^{1,3}, QINGFA ZENG², FEI YANG^{1,3}, BIN LIN^{1,3}, OUYANG XU^{1,3},
AND YUANBIN HE², (Member, IEEE)

¹Key Laboratory of Far-Shore Wind Power Technology of Zhejiang Province, Hangzhou 310005, China

²Engineering Laboratory of Regional Energy Internet, Zhejiang Province, Hangzhou Dianzi University, Hangzhou 310018, China

³PowerChina Huadong Engineering Corporation Ltd., Hangzhou 310048, China

Corresponding author: Yuanbin He (yuanbinhe@hdu.edu.cn)

This work was supported in part by the Key Laboratory of Far-Shore Wind Power Technology of Zhejiang Province under Grant ZOE2021002, and in part by the Key Research and Development Program of Zhejiang under Grant 2023C01227.


ABSTRACT A digital controlled unipolar hysteresis current control strategy applied to the single-phase grid-connected inverter is studied in the paper. In view of the problem of current zero-crossing distortion in the traditional unipolar hysteresis current control based on finite state machines (FSM), a new unipolar hysteresis current control strategy based on current decoupling is proposed. By introducing a virtual zero-sequence current, the single-phase full-bridge inverter is decoupled into two independent half-bridge inverter units, which are controlled by two bipolar hysteresis current control loops under the constraints of a finite state machine. Therefore, the operation rules of the FSM ensure the frequency doubling output of the unipolar modulation, and the virtual two-phase decoupled current eliminates the zero-crossing distortion problem of inverter output current. Finally, the effectiveness and feasibility of the proposed method were verified by building a 1kW single-phase full-bridge grid-connected inverter in the laboratory.

INDEX TERMS Grid-connected inverter, unipolar modulation, hysteresis, finite state machine, current decoupling.

I. INTRODUCTION

Photovoltaic power generation is one of the most rapidly developing renewable energy power generation technologies in recent years [1], [2]. As the core component of photovoltaic power generation, the control performance of grid-connected inverters is related to the stability and the power quality of the entire grid-connected system [3]. Therefore, choosing a suitable grid-connected inverter control method is of great significance to the efficient and stable operation of photovoltaic power generation systems.

The control methods for grid-connected inverters are mainly divided into two categories: linear control [4], [5], [6], [7] and nonlinear control [8], [9], [10], [11], [12], [13], [14], [15], [16], [17], [18], [19], [20], [21], [22], [23], [24], [25].

The associate editor coordinating the review of this manuscript and approving it for publication was Kuo-Lung Lian .

The linear controllers of single-phase grid-connected inverters mainly include proportional integration (PI) controller [4], proportional resonance (PR) controller [5], repetitive controller [6], and deadbeat controller [7]. Among them, PI and PR controllers are commonly used because of their simplicity and reliability. Although PI and PR controllers are preferred in grid-connected inverter systems, they need to design parameters carefully based on small-signal AC models, and their dynamic performance is limited [8]. Especially under the conditions of weak power grids, the closed-loop bandwidth based on linear control decreases rapidly, causing interactive coupling between the inner and outer loops, which can easily deteriorate the dynamic performance, and even lead to stability problems. On the contrary, nonlinear control has better dynamic performance and global stability [9]. The nonlinear control strategies of single-phase inverters mainly include hysteresis current control (HCC) [8], [9], [10],

[11], [12], [13], [14], [15], [16], [17], [18], [19], [20], [21], sliding mode control [22], second-order boundary control [23], and direct power control [24]. Among them, hysteresis current control has the advantages of fast response speed, good robustness, built-in current limiting function, and easy implementation. Owing to the advanced digital processing technologies, the digital implementation of the HCC becomes very simple. Thus, the HCC has been widely used in practical applications of voltage source inverters [8], [9], [10], [11], [12], [13], [14], [15], [16], [17], [18], [19], [20], [21].

The HCC for single-phase grid-connected inverters is mainly divided into bipolar HCC [9], [10], [11], [12] and unipolar HCC [14], [15], [16], [17]. Bipolar HCC corresponds to bipolar sinusoidal pulse width modulation (BSPWM), while unipolar HCC corresponds to unipolar sinusoidal pulse width modulation (USPWM). Compared with bipolar HCC, unipolar HCC is more widely used due to smaller inductance volt-second product and switching harmonics [14], [17]. Unipolar HCC is usually divided into asymmetric unipolar HCC [14], [15] and symmetric unipolar HCC [16], [17]. Although both can achieve three-level output voltage, compared with asymmetric unipolar HCC, symmetric unipolar HCC can achieve the effect of frequency doubling and is preferable in practical applications [25], [26]. Symmetrical USPWM has four switching combination states, two of which correspond to the zero-voltage level and are called as zero vectors. Therefore, the timing positions of the zero vectors need to be interspersed between non-zero vectors. Currently, the logic gates (e.g., JK flip-flops) and finite state machine (FSM) are commonly used to realize the interspersing of zero vectors [16], [17], [20]. However, the traditional unipolar HCC has current distortion when the output voltage crosses the zero point [14]. To this end, authors in [14] propose a lead phase compensation to alleviate the current zero-crossing distortion. However, this method relies on circuit parameters, and is prone to over-compensation or under-compensation. There are also some literatures that present hybrid PWM methods to solve the problem of current zero crossing distortion [8], [18], that is, BSPWM is used near the zero crossing, and USPWM is used for the rest. However, this hybrid modulation method would increase the switching ripple of current at the zero crossing.

The main motivation of this paper is to use a digital decoupled hysteresis current control strategy to address the current zero-crossing distortion problem of unipolar HCC. Based on the concept of current decoupling, the single-phase full-bridge inverter is decoupled into two independent half-bridge inverter units, and the bipolar hysteresis current control is used to regulate two half-bridge units separately according to the state machine rules, thereby eliminating the current zero-crossing distortion.

The main structure of the article is as follows. Sec. II introduces the principle of the traditional unipolar HCC based on finite state machines, and analyzes the causes of current zero-crossing distortion. Sec. III introduces the principle of current decoupling and decoupled hysteresis current control. The

experimental verification is conducted in Sec. IV. Finally, the conclusion is given.

II. TRADITIONAL UNIPOLAR HCC STRATEGY BASED ON FINITE STATE MACHINE

A. SYMMETRIC UNIPOLAR SPWM STRATEGY

For simplicity, a single-phase full-bridge grid-connected inverter based on an L-type filter shown in Fig. 1 is taken as the main circuit structure in the following analysis, where U_d is the DC bus voltage, C_d is the DC capacitor, $Q_1 \sim Q_4$ are the switching devices, u_{inv} means the output voltage of the inverter, L_1 is the output filter inductor, i_L is the inductor current, and u_g represents the grid voltage.

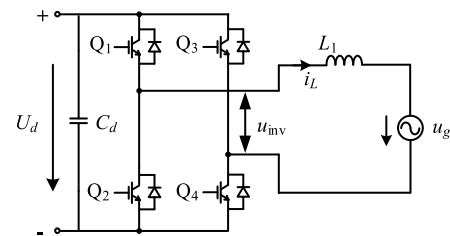


FIGURE 1. Single-phase full-bridge grid-connected inverter.

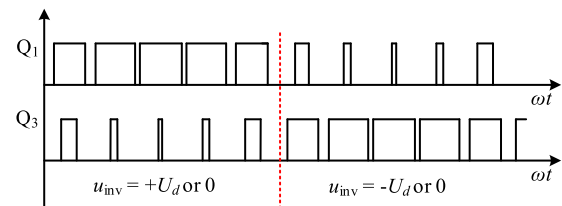


FIGURE 2. Switching signals of USPWM.

Fig. 2 shows the driving signals of unipolar SPWM, the corresponding switching sequence is given in Table 1. Let $Q_x = 1$ ($x = 1, 2, 3, 4$) indicate that the switching device Q_x is turned on, and $Q_x = 0$ indicate that the switching device Q_x is turned off. As seen from Table 1, switching states of 00 and 11 mean zero vectors, and 01 and 10 mean non-zero vectors. Zero vectors 00 and 11 alternate.

TABLE 1. Switching sequence of USPWM.

Polarity of grid voltage	Switching state of Q_1Q_3
positive	10,11,10,00,10,11,10,00...
negative	01,11,01,00,01,11,01,00...

B. ANALYSIS OF CURRENT ZERO-CROSSING DISTORTION

The FSM are commonly used to realize the interspersing of zero vectors in power converter modulation [16], [25]. Fig. 3 presents the circuit state transformation of the unipolar HCC based on the finite state machine.

With unipolar HCC, the switching ripple current near the zero crossing approaches zero, that is, the intracycle change

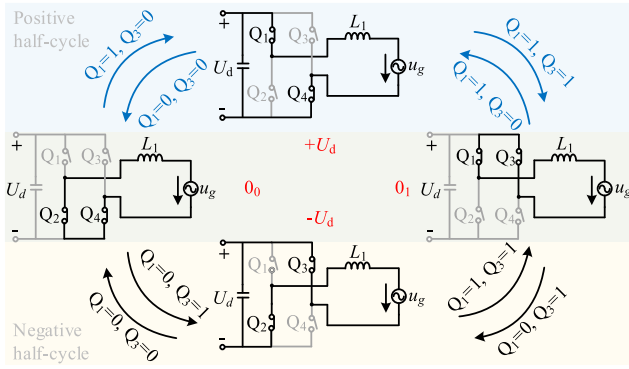


FIGURE 3. Circuit state transformation of FSM-based unipolar HCC.

slope of the inductor current might be less than the change slope of the reference current. Then, the hysteresis current control based on the finite state machine will cause the current to be distorted near the zero crossing. The following will analyze the causes of current zero-crossing distortion in detail.

According to Fig. 3, it is derived that the relationship between circuit variable and the switching state is

$$u_g(t) \geq 0 : \begin{cases} u_{inv}(t) = 0 & Q_1Q_3 = 00 \text{ or } 11 \\ u_{inv}(t) = U_d & Q_1Q_3 = 10 \end{cases} \quad (1a)$$

$$u_g(t) < 0 : \begin{cases} u_{inv}(t) = 0 & Q_1Q_3 = 00 \text{ or } 11 \\ u_{inv}(t) = -U_d & Q_1Q_3 = 01 \end{cases} \quad (1b)$$

and the inductance terminal voltage expression is obtained from Kirchhoff voltage law (KVL)

$$v_L(t) = L_1 \frac{di_L(t)}{dt} = u_{inv}(t) - u_g(t) \quad (2)$$

If the output current of the inverter is in phase with the grid voltage, then

$$\begin{cases} u_g(t) = U_m \sin(\omega t) \\ i_{L,ref}(t) = I_m \sin(\omega t) \end{cases} \quad (3)$$

where U_m and I_m are the grid voltage and reference current amplitudes, respectively, and ω is the grid angular frequency. Combining (1) to (3), the intracycle change rate of the inductor current in different switching states is obtained

$$\frac{di_L(t)}{dt} = \frac{1}{L_1} \begin{cases} U_d - U_m \sin(\omega t) & Q_1Q_3 = 10 \\ -U_m \sin(\omega t) & Q_1Q_3 = 00 \text{ or } 11 \\ -U_m \sin(\omega t) - U_d & Q_1Q_3 = 01 \end{cases} \quad (4)$$

Fig. 4 shows the working principal diagram of the unipolar HCC near the zero crossing, where the waveforms on the left shows the current from the positive half cycle to the negative half cycle at $\omega t = 180^\circ$, and the waveforms on the right shows the current from the negative half cycle to the positive half cycle at $\omega t = 0^\circ$. The switching logic in the figure is determined by the operation instructions of the finite state machine. It can be seen from the figure that before crossing

the zero crossing, the inductor current cannot be reduced to zero due to the long-term sliding outside the hysteresis band. As a result, the current is distorted near the zero crossing.

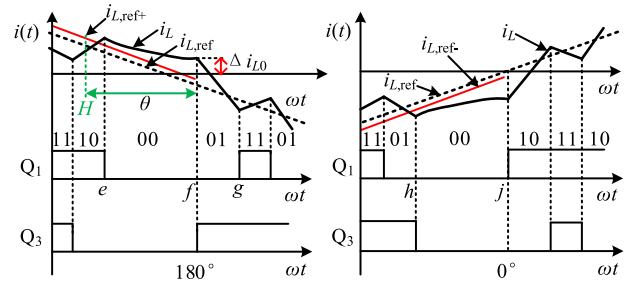


FIGURE 4. Schematic diagram of current zero-crossing distortion under unipolar HCC.

Taking ωt approaching 180° as an example, the cause of the zero-crossing distortion is mathematically calculated in the following. First, the change rate of the reference current is obtained

$$\frac{di_{L,ref}}{dt} = \omega I_m \cos(180^\circ - \theta) \quad (5)$$

At the zero crossing, the change rate of the reference current reaches the maximum value ωI_m . However, it can be seen from (4) that the intracycle change rate of the actual inductor current is

$$\frac{di_L(t)}{dt} = \frac{1}{L_1} \begin{cases} U_d - U_m \sin(\omega t) & Q_1Q_3 = 10 \\ -U_m \sin(\omega t) & Q_1Q_3 = 00 \text{ or } 11 \end{cases} \quad (6)$$

When ωt approaches 180° , the rising slope of the inductor current gradually increases and the falling slope gradually decreases. In theory, when the zero crossing is reached, the falling slope of the actual inductor current will drop to 0. On the left side of Fig. 4, $i_L > i_{L,ref+}$ is detected at point e , then $Q_1Q_3 = 00$, and the inductor current drops. However, since the falling slope of the actual inductor current is always smaller than the falling slope of the reference current, the inductor current in the ef interval cannot follow the reference value.

In order to calculate the distortion value of the inductor current, set point H in Fig. 4, and θ between point H and $\omega t = 180^\circ$ is named as the distortion angle. Moreover, assume that the descending slope of the actual inductor current at this point equals the change slope of the reference current, that is,

$$\frac{di_L(t)}{dt} = \frac{di_{L,ref}(t)}{dt} = \frac{-U_m \sin(180^\circ - \theta)}{L_1} \quad (7)$$

By solving (5) and (7), it obtains

$$\theta = \arctan \frac{L_1 I_m \omega}{U_m} \quad (8)$$

It can be seen from (8) that, as the filter inductance value becomes larger or the output current amplitude increases, the distortion angle θ increases.

If the sampling point occurs at point H , the falling slope of the actual inductor current from point H will be less than

the change rate of the reference current. Accordingly, the inductor current begins to deviate from the reference current. When the zero crossing is reached, the amplitude of the inductor current deviating from the reference current reaches the maximum value $\Delta i_{L0,max}$. Combining (6) and (7), the maximum deviation value is obtained

$$\Delta i_{L0,max} \approx \frac{I_m^2 L_1 \omega}{\sqrt{U_m^2 + (I_m L_1 \omega)^2}} + \frac{U_m}{L_1 \omega} \left[\frac{U_m}{\sqrt{U_m^2 + (I_m L_1 \omega)^2}} - 1 \right] \quad (9)$$

The above formula shows the distortion of the inductor current when it crosses the zero point of the inverter output voltage.

When the reference current reaches zero, the finite state machine enters a negative half cycle. Since $i_L > i_{L,ref+}$, $Q_1 Q_3 = 01$. Then, the change slope of the actual inductor current becomes

$$\frac{di_L(t)}{dt} = \frac{-U_m \sin(\omega t) - U_d}{L_1} \approx \frac{-U_d}{L_1} \quad (10)$$

At this time, it is satisfied that the change slope of the actual inductor current is greater than the slope of the reference current, and the inductor current changes in accordance with the hysteresis trajectory.

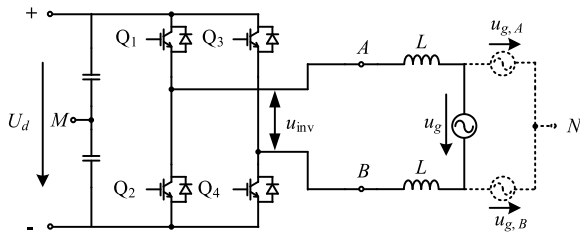


FIGURE 5. Single-phase full-bridge inverter by splitting grid voltage.

III. PROPOSED UNIPOLAR HCC BASED ON CURRENT DECOUPLING

This section will propose a new type of unipolar HCC based on current decoupling, which is used to eliminate the current zero-crossing distortion of unipolar HCC. The idea of current decoupling was first introduced in the direct power control of three-phase inverters [27], but the switching state machine model between phases is not considered. As a result, it may lose the switching frequency doubling effect between phases and cannot be directly used for unipolar HCC. This section will first analyze the basic principles of current decoupling, and then eliminate current zero-crossing distortion and realize switching frequency doubling effect by combining current decoupling and finite state machine.

A. CURRENT DECOUPLING PRINCIPLE BASED ON SINGLE-PHASE FULL-BRIDGE INVERTER

The single-phase full-bridge inverter can be regarded as two single-phase half-bridge sub-units, which are coupled with

each other. The idea of current decoupling is to decouple them into two independent half-bridge sub-units. Decompose the inductance L_1 in Fig. 1 into two inductors, L , and the grid voltage u_g is divided into two virtual AC voltage sources $u_{g,A}$ and $u_{g,B}$. Then, based on Fig. 5, it has

$$\begin{cases} u_g = u_{g,A} - u_{g,B} \\ u_{g,A} = -u_{g,B} \end{cases} \quad (11)$$

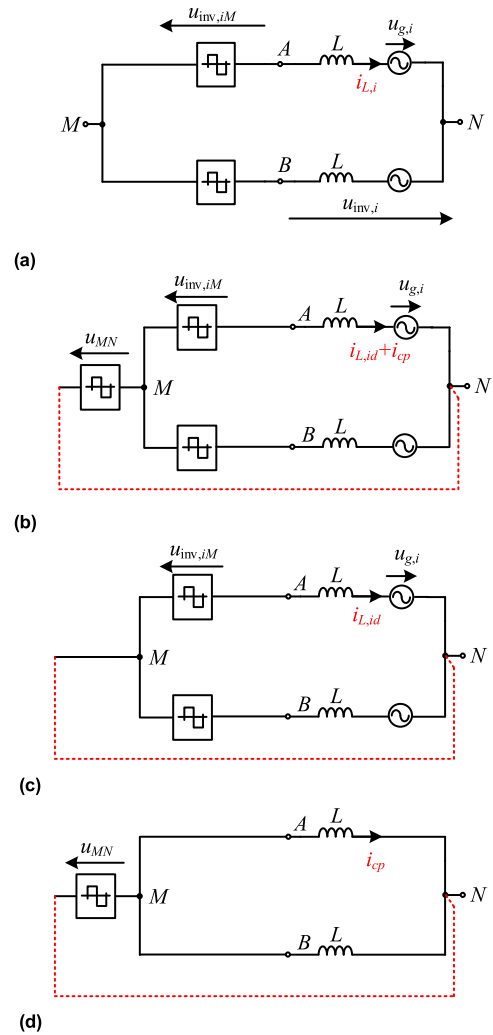


FIGURE 6. Equivalent circuit of single-phase full-bridge inverter. (a) Equivalent circuit I. (b) Equivalent circuit II. (c) Equivalent sub-circuit I with differential-mode current. (d) Equivalent sub-circuit II with common-mode current.

In order to illustrate the decoupling process of a single-phase full-bridge inverter, the circuit of Fig. 5 is equivalent to the circuit of Fig. 6(a), where $u_{inv,iM}$ ($i = A, B$) represents the AC output voltage of the inverter with the midpoint of the DC bus voltage M as the reference point, $i_{L,i}$ represents the inductor current, $u_{g,i}$ represents the virtual grid voltage, and $u_{inv,i}$ is the AC voltage with the virtual midpoint N of the grid voltage as the reference point. The relationship between two

phase current meets

$$i_{L,A} = -i_{L,B} \quad (12)$$

The differential equation of the inductor current is

$$\begin{cases} L \frac{di_{L,A}}{dt} = u_{L,A} = u_{inv,A} - u_{g,A} \\ L \frac{di_{L,B}}{dt} = u_{L,B} = u_{inv,B} - u_{g,B} \end{cases} \quad (13)$$

Define the voltage between the midpoint M of the DC bus voltage and the virtual midpoint N of the grid voltage is the voltage u_{MN} . Then, the circuit of Fig. 6(a) is equivalent to the circuit shown in Fig. 6(b), and

$$\begin{cases} u_{inv,A} = u_{inv,AM} + u_{MN} \\ u_{inv,B} = u_{inv,BM} + u_{MN} \end{cases} \quad (14)$$

where u_{MN} is the common-mode voltage and $u_{inv,iM}$ ($i = A, B$) means the differential-mode voltage. The inductor current $i_{L,i}$ in (13) is related to both of them. Assume that the inductor current is composed of two parts: the one is the decoupled differential-mode inductor current $i_{L,id}$, and the other is the virtual common-mode inductor current i_{cp} . It has

$$i_{L,id} = i_{L,i} + i_{cp} \quad (i = A, B) \quad (15)$$

Then, Eq. (13) is rewritten as

$$\begin{cases} L \frac{di_{L,Ad}}{dt} + L \frac{di_{cp}}{dt} = (u_{inv,AM} - u_{g,A}) + u_{MN} \\ L \frac{di_{L,Bd}}{dt} + L \frac{di_{cp}}{dt} = (u_{inv,BM} - u_{g,B}) + u_{MN} \end{cases} \quad (16)$$

Further, it has

$$\begin{cases} L \frac{di_{L,Ad}}{dt} = u_{inv,AM} - u_{g,A} \\ L \frac{di_{L,Bd}}{dt} = u_{inv,BM} - u_{g,B} \end{cases} \quad (17a)$$

$$L \frac{di_{cp}}{dt} = u_{MN} \quad (17b)$$

Therefore, the circuit of Fig. 6(b) can be decomposed into the decoupled differential-mode equivalent circuit of Fig. 6(c) and the common-mode equivalent circuit of Fig. 6(d).

Based on (17b), the virtual current i_{cp} is obtained from

$$i_{cp} = \frac{1}{L} \int u_{MN} dt \quad (18)$$

where u_{MN} can be derived based on (11) to (14).

$$u_{MN} = -\frac{1}{2}(u_{inv,AM} + u_{inv,BM}) \quad (19)$$

After decoupling two-phase inductor current, the equivalent differential-model inverter circuit is presented in Fig. 7.

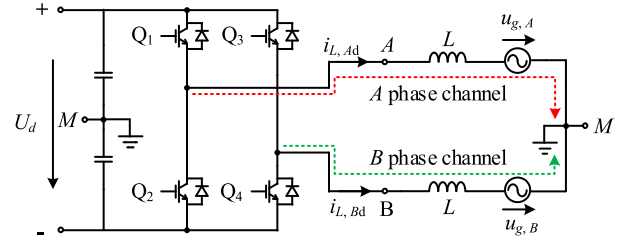


FIGURE 7. Equivalent inverter circuit with current decoupling.

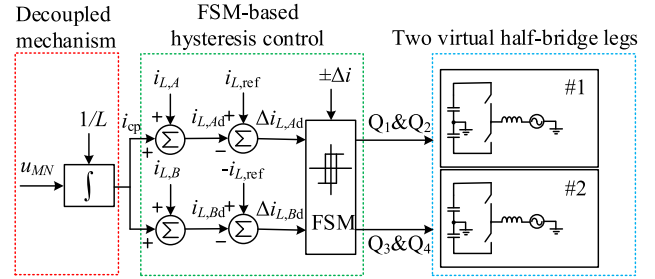


FIGURE 8. Control structure diagram of current decoupling-based HCC.

B. PRINCIPLE OF UNIPOLAR HCC BASED ON CURRENT DECOUPLING

Fig. 8 shows the control structure diagram of the unipolar HCC based on current decoupling between phases A and B. The specific implementation process is

(1) Obtain the high-frequency zero-sequence current according to (18).

(2) Superimpose the coupling current on the actual inductor current to obtain the decoupled two-phase virtual inductor current.

(3) Switching sequence and switching action time are constrained by the finite state machine and the virtual decoupling inductor current.

Since the common-mode voltage value is involved in (18), u_{MN} needs to be predicted during actual execution. From (19), the common-mode voltage u_{MN} is determined by the output voltage of the two half-bridge sub-units. For example, when $Q_1Q_3 = 11$, $u_{inv,iM} = U_d/2$; when $Q_1Q_3 = 00$, $u_{inv,iM} = -U_d/2$. Otherwise, $u_{inv,iM} = 0$. A module that predicts the common-mode voltage u_{MN} based on the switching state, is given in Fig. 9.

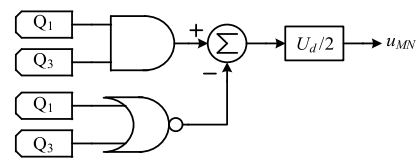


FIGURE 9. Prediction module of common-mode voltage.

Combined with the virtual half-bridge output level of the grid voltage, an HCC working principal diagram based on the virtual inductor current can be drawn, as shown in Fig. 10.

It can be seen from the figure that after the actual inductor current is decoupled into a two-phase virtual inductor current, the upper and lower boundaries of the reference current are compared separately, and the switching action is determined under the constraints of the finite state machine. Combined with Fig. 7, it is derived that, after decoupling, the intracycle change rate of the virtual inductor current is

$$\begin{cases} L \frac{di_{L,id}}{dt} = \frac{U_d}{2} - u_{g,i} & Q_1 = 1 \text{ or } Q_3 = 1 \\ L \frac{di_{L,id}}{dt} = -\frac{U_d}{2} - u_{g,i} & Q_1 = 0 \text{ or } Q_3 = 0 \end{cases} \quad (20)$$

Then, the intracycle ripple of virtual inductor current near the zero crossing no longer approaches zero as shown in Fig. 10, and the change rate of the inductor current is no longer less than the change rate of the reference current, which is the reason of current distortion near the zero crossing as analyzed in Sec. II-B. Based on (20), the switching frequency is regulated based on the following variable hysteresis band

$$\Delta I = \frac{U_d^2 - u_g^2}{8Lf_{sw}^* U_d} \quad (21)$$

where f_{sw}^* means the desired switching frequency.

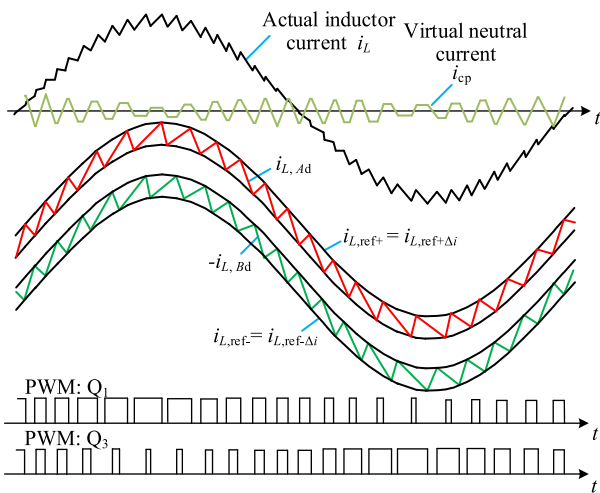


FIGURE 10. Schematic diagram of unipolar HCC based on virtual inductor current.

As can be seen from Fig. 10, during the entire line cycle of the inverter, the switching actions of the two virtual half-bridge sub-circuits after decoupling are still constrained by the finite state machine as shown in Fig. 3, and the drive signals of Q_1 and Q_3 maintain central symmetry.

IV. SIMULATION RESULTS

Based on the circuit parameters tabulated in Table 2 and the circuit topology in Fig. 13, the USPWM inverter performance based on the traditional linear PI controller, FSM HCC, and the proposed decoupled HCC is compared in the computer simulation. For the sake of fair comparison, both voltage and current signals are sampled at multiple frequencies (e.g., 400kHz).

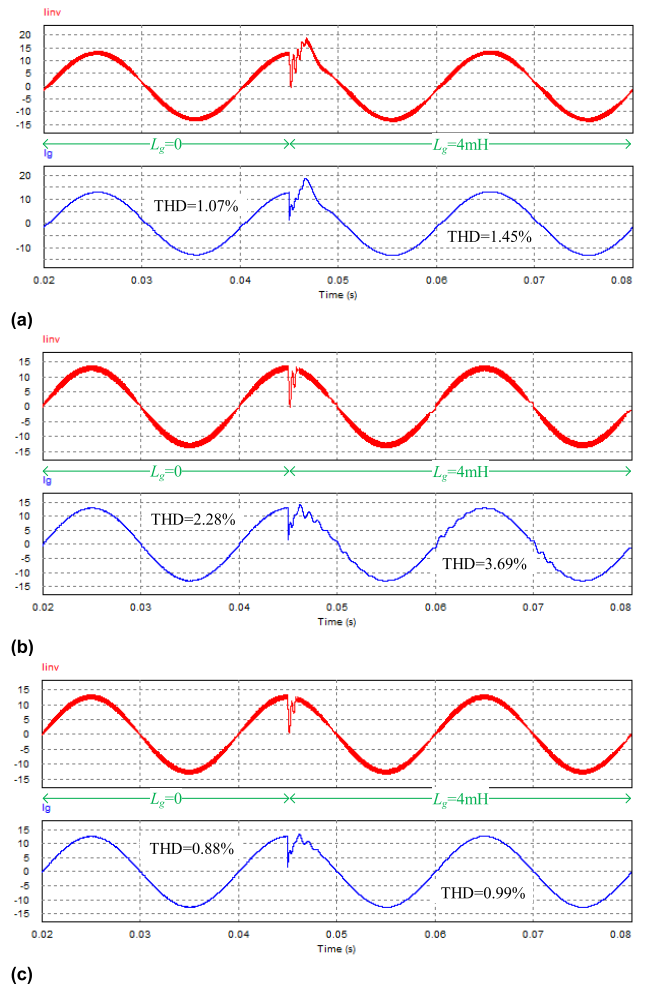


FIGURE 11. Comparative simulation waveforms of the USPWM inverter under different grid inductance. (a) Linear PI control. (b) FSM HCC. (c) Proposed decoupled HCC.

Fig. 11 compares the inverter stability with the change of equivalent grid inductance. As seen in Fig. 11(a), the inverter with linear PI controller keeps stable with the increase of grid inductance from 0 to 4mH. However, the total harmonic distortion rate (THD) of the grid current increases from 1.07% to 1.45% because the control loop gain reduces with the increase of L_g , which causes the decrease of harmonic suppression capability. As seen in Fig. 11(b), the stability of the inverter with FSM HCC becomes weak with the increase of grid inductance. The current oscillation near the zero crossing is amplified, that is because the switching frequency near the zero crossing is close to the resonant frequency of the filter. In comparison, the inverter with the proposed decoupled HCC addresses the problem of grid current distortion near the zero crossing, and has an ultra-wide control loop gain compared with linear control technique [23]. Thus, it not only keeps stable with the increase of grid inductance, but also has the lowest THD of grid current.

It should be noted that, in practical applications, although the traditional linear control with multisampling technique

is proven to achieve high operational stability both in the stiff and weak grid conditions, the multisampling PWM still faces the challenges of deadband effect and multiple crossing between carrier and modulation wave [28].

V. EXPERIMENTAL VERIFICATION

In order to verify the feasibility and effectiveness of the proposed current decoupling-based HCC, a prototype of a 1kW single-phase grid-connected inverter with an LCL filter is built in this section. The specific experimental parameters are tabulated in Table 2. The experimental platform is shown in Fig. 12.

TABLE 2. Key parameters in experiments.

SYMBOL	VALUE
DC bus voltage U_d	200V
Inverter-side inductance L_1	1.4mH
Filter capacitance C_f	4.7 μ F
Grid-side inductance L_g	0.4mH
Grid voltage u_g	110Vrms/50Hz
Rated power P_o	1kW
Sampling frequency f_s	400kHz
Deadtime T_d	1 μ s

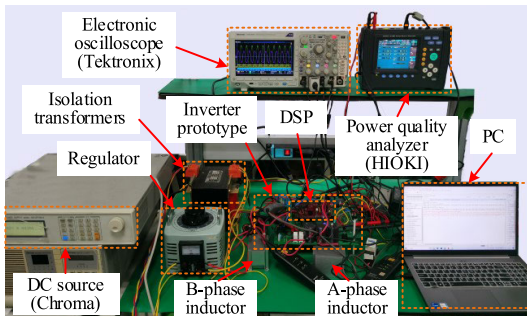


FIGURE 12. Experimental platform.

Fig. 13 shows the structure diagram of the power stage and control stage, where the r_1 , r_g , and r_c in the power stage are the parasitic resistors of the corresponding filter components, and pcc means the point of common coupling (PCC). The control stage is mainly composed of two interrupt service programs running in parallel:

(1) A 40kHz low-frequency interrupt service program in the main CPU, which mainly performs operations that do not require high calculation rate such as reference current calculation, hysteresis band calculation, phase-locked loop (PLL), etc.;

(2) A 400kHz high-frequency operation program in the control law accelerator (CLA), which mainly performs core algorithm operations such as current decoupling, state machine, and generating the PWM signal.

The core hysteresis algorithm in the CLA is concise and only requires about 1.9 μ s execution time, so the high-frequency interrupt service program does not require high-speed CPU.

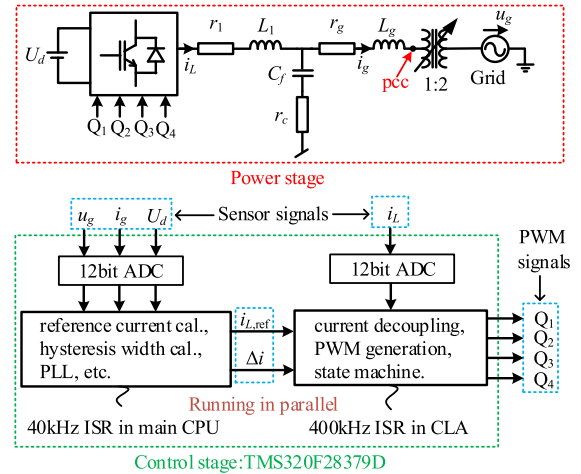


FIGURE 13. Structure diagram of the key parts of power stage and control stage.

A. EXPERIMENTAL RESULTS BASED ON FINITE STATE MACHINES

Fig. 14(a) shows the inverter-side inductor current and pcc voltage waveforms based on the traditional unipolar HCC. The amplified waveforms near the zero crossing are shown in Fig. 14(b), where u_{g1} and u_{g3} are the corresponding drive signals. As can be seen from Fig. 14(b), the switching state is strictly in accordance with the USPWM operation rules. However, the change rate of the inductor current near the zero crossing approaches zero, so the inductor current is distorted. This is consistent with the theoretical analysis. At the same time, the switching frequency drops abruptly to 1.8kHz, and causes the distortion of grid current as shown in Fig. 14(c). Such distortion may even cause resonance amplification when the switching frequency near the zero crossing is close to the filter resonant frequency, which poses a threat to the safety and stability of the system. The THD of the grid current in Fig. 14(c) is 3.95%.

Although the switching frequency control of FSM has been carried out through the variable hysteresis loop width in the algorithm, the performance of switching frequency control is very poor due to the inductor current ripple of the USPWM approaching zero near the zero crossing, as shown in Fig. 15. Such wide-ranging change in switching frequency makes the design of filter parameters very difficult, and it is easy to cause harmonic stability problems.

B. EXPERIMENTAL RESULTS BASED ON CURRENT DECOUPLING

Fig. 16(a) shows the inverter-side inductor current and pcc voltage waveforms of the proposed HCC based on current decoupling. The amplified waveforms near the zero crossing are shown in Fig. 16(b). As seen from Fig. 16(b), after adding current decoupling mechanism, the hysteresis current control can still maintain unipolar operation. Moreover, the inductor current near the zero crossing tracks the reference current well, there is no sudden drop in the switching frequency, and

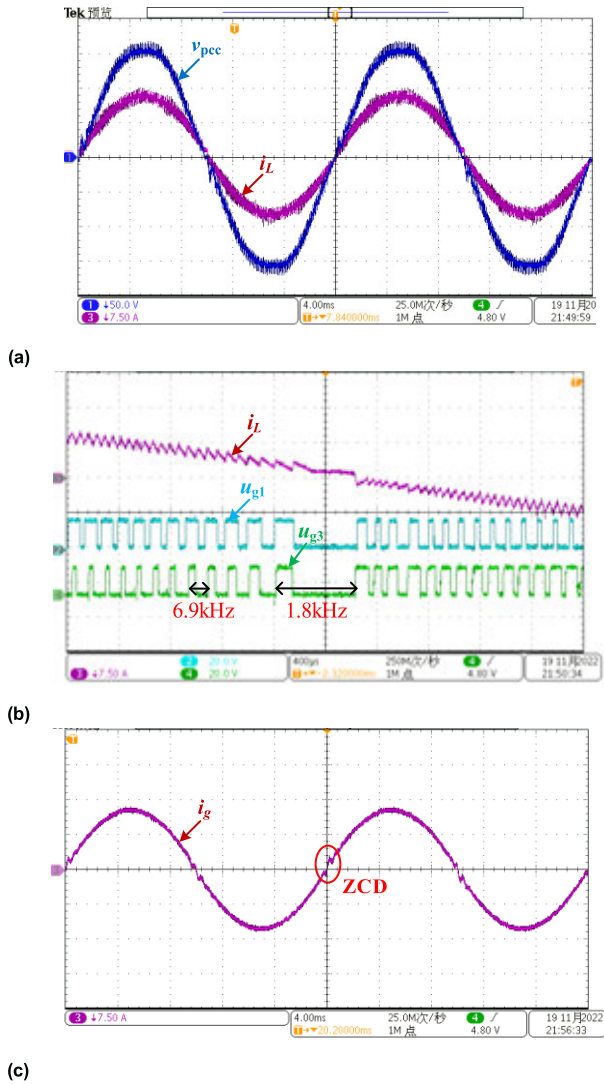


FIGURE 14. Key waveforms based on the traditional FSM. (a) Inductor current and pcc voltage waveforms. (b) Inductor current waveform and drive signals near the zero crossing. (c) Grid current waveform.

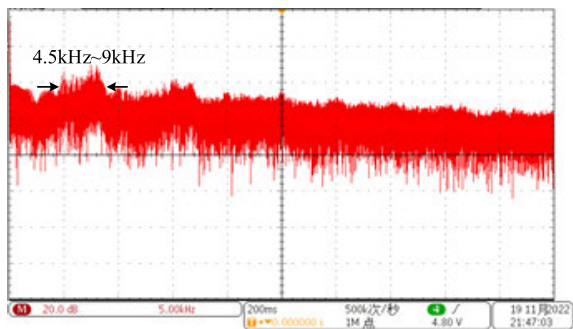


FIGURE 15. Frequency spectrum of PWM wave in the traditional FSM.

the inductor current smoothly transits from a positive half cycle to a negative half cycle. Fig. 16(c) shows the waveforms of the grid current. It is seen from the figure that there is no

distortion of the grid current during the zero crossing. The THD of the grid current is only 1.45%.

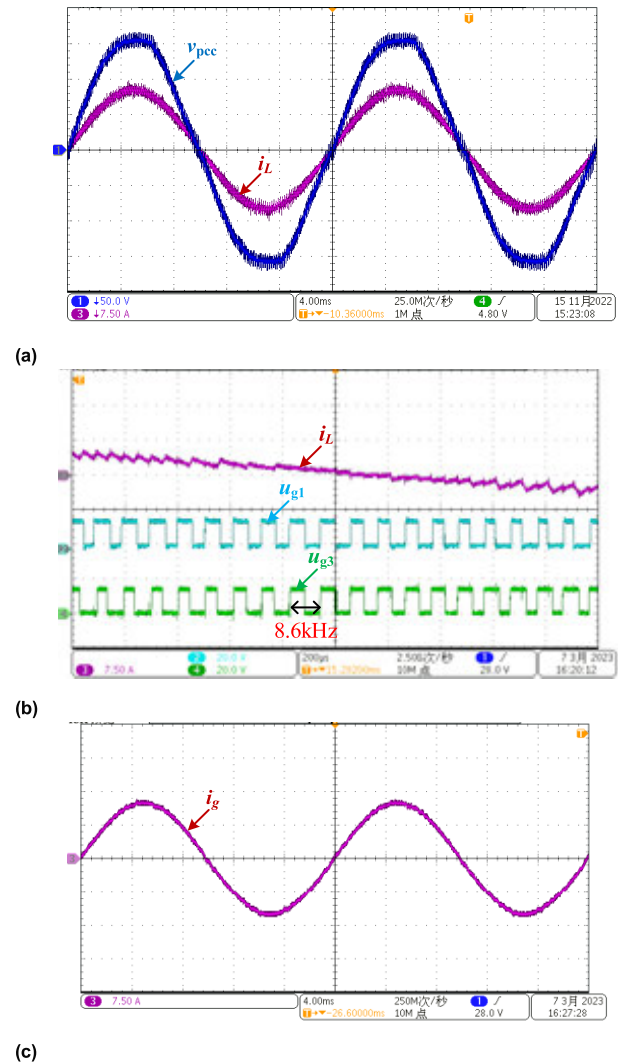


FIGURE 16. Key waveforms based on the proposed decoupled method. (a) Inductor current and pcc voltage waveforms. (b) Inductor current waveform and drive signals near the zero crossing. (c) Grid current waveform.

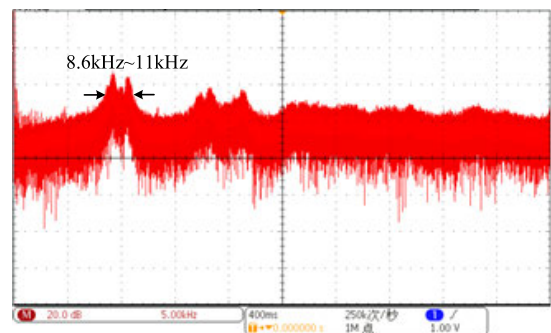


FIGURE 17. Frequency spectrum of PWM wave in the proposed decoupled method.

The performance of switching frequency control based on the proposed decoupling HCC is shown in Fig. 17.

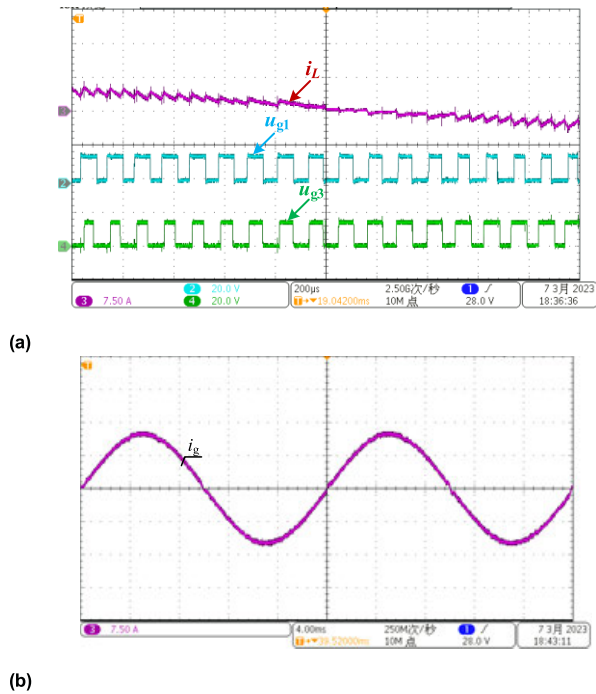


FIGURE 18. Waveforms of the proposed decoupled method with negative drifting of the inverter-side inductance drift. (a) Waveforms near the zero crossing. (b) Grid current waveform.

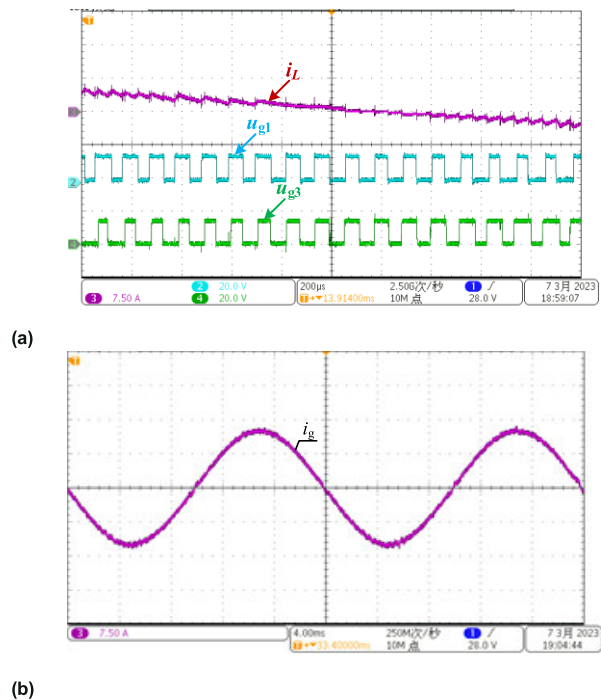


FIGURE 19. Waveforms of the proposed decoupled method with positive drifting of the inverter-side inductance drift. (a) Waveforms near the zero crossing. (b) Grid current waveform.

Compared with Fig. 15, the proposed method has much better control effect on the switching frequency. It should be noted that, the mean switching frequency will not change as

the output power varies, and the performance of switching frequency control can be further improved by closed-loop adjustment [23].

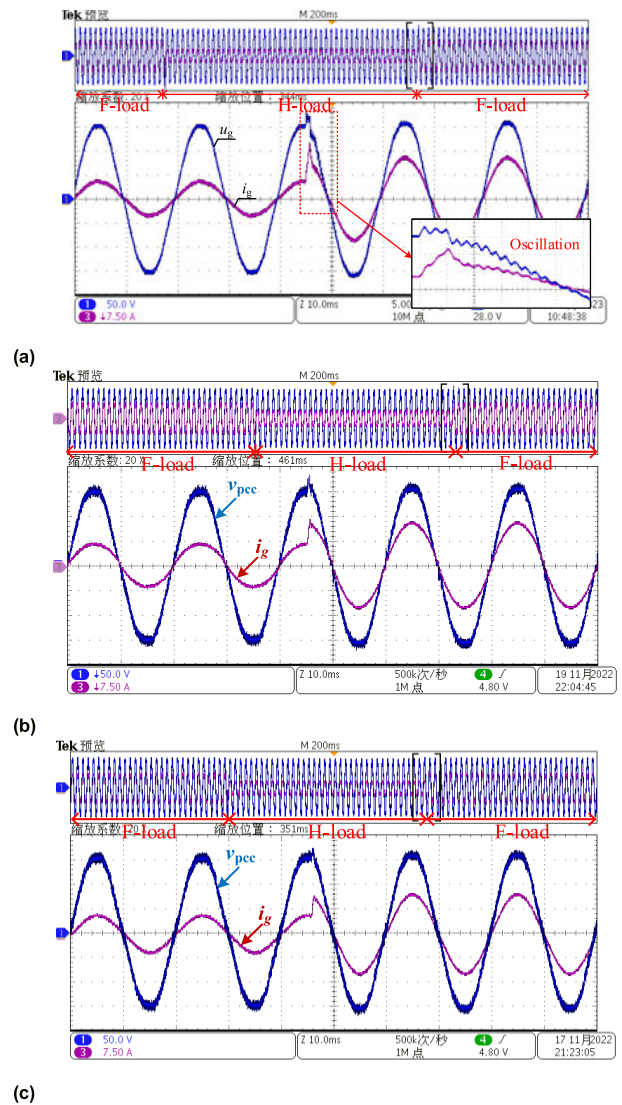


FIGURE 20. Transient response comparison by increasing reference current. (a) Waveforms with the linear control. (b) Waveforms with the finite state machine. (c) Waveforms with the current decoupling.

In order to verify the influence of inverter-side inductance drift on the control performance of current decoupling, the following experiments are carried out.

(1) Negative drifting of the inductance: The inductance value of phase A is 0.49mH, and the inductance value of phase B is 0.59mH. The total inductance value is negatively offset by 23%, and the corresponding experimental waveforms are shown in Fig. 18. It can be seen from the figure that the inductor current is not distorted. The THD of the grid current is 1.68%.

(2) Positive drifting of the inductance: The inductance value of phase A is 0.98mH, and the inductance value of phase B is 0.75mH. The total inductance value is positively

offset by 23.6%, and the corresponding experimental waveforms are shown in Fig. 19. It can be seen from the figure that the inductor current is not distorted. The THD of the grid current is 1.53%.

Based on the above comparison, it can be seen that the digital HCC based on current decoupling has a good adaptability to the inductance drift. Even when the power inductance drifts in a wide range, the proposed HCC can still maintain stable.

Finally, the transient response comparison by increasing the reference current is carried out. As shown in Fig. 20, both of the unipolar HCC with the finite state machine and the proposed current decoupling have much better dynamic response and much smaller current overshoot than the traditional linear control.

VI. CONCLUSION

The paper proposes a current decoupling-based unipolar hysteresis current control strategy applied to a single-phase grid-connected inverter. The reason of current zero-crossing distortion in the traditional FSM-based HCC is analyzed. It is found that when the intracycle change slope of the inductor current is less than the slope of the reference current near the zero crossing, the inductor current will be distorted. Therefore, by introducing a virtual two-phase decoupled current, the intracycle change rate of the inductor current near the zero crossing is increased, and the distortion of the current is eliminated. Finally, a 1kW single-phase grid-connected inverter prototype was built in the laboratory to verify that the proposed control strategy effectively solves the current zero-crossing distortion problem of unipolar HCC under the premise of inheriting the excellent dynamic performance of hysteresis current control, and has a strong adaptability to the drift of inductance parameters.

REFERENCES

- [1] F. Chishty, S. Murshid, and B. Singh, "Frequency adaptive multistage harmonic oscillator for renewable-based microgrid under nonideal grid conditions," *IEEE Trans. Ind. Electron.*, vol. 68, no. 1, pp. 358–369, Jan. 2021.
- [2] H. A. Gabbar, M. R. Abdussami, and Md. I. Adham, "Optimal planning of nuclear-renewable micro-hybrid energy system by particle swarm optimization," *IEEE Access*, vol. 8, pp. 181049–181073, 2020.
- [3] J. L. Sosa, M. Castilla, J. Miret, J. Matas, and Y. A. Al-Turki, "Control strategy to maximize the power capability of PV three-phase inverters during voltage sags," *IEEE Trans. Power Electron.*, vol. 31, no. 4, pp. 3314–3323, Apr. 2016.
- [4] H. Komurcugil, S. Bayhan, F. Bagheri, O. Kukrer, and H. Abu-Rub, "Model-based current control for single-phase grid-tied quasi-z-source inverters with virtual time constant," *IEEE Trans. Ind. Electron.*, vol. 65, no. 10, pp. 8277–8286, Oct. 2018.
- [5] P. Alemi, C.-J. Bae, and D.-C. Lee, "Resonance suppression based on PR control for single-phase grid-connected inverters with LLCL filters," *IEEE J. Emerg. Sel. Topics Power Electron.*, vol. 4, no. 2, pp. 459–467, Jan. 2016.
- [6] F. Xu, M. Zhu, and Y. Ye, "The stability of LCL-type grid-tied inverter based on repetitive control and grid voltage feed-forward," *IEEE J. Emerg. Sel. Topics Power Electron.*, vol. 11, no. 2, pp. 1496–1506, Apr. 2023.
- [7] H. Heydari-doostabad and M. Monfared, "An integrated interleaved dual-mode time-sharing inverter for single-phase grid-tied applications," *IEEE Trans. Ind. Electron.*, vol. 66, no. 1, pp. 286–296, Jan. 2019.
- [8] H. Yi, F. Zhuo, F. Wang, and Z. Wang, "A digital hysteresis current controller for three-level neural-point-clamped inverter with mixed-levels and prediction-based sampling," *IEEE Trans. Power Electron.*, vol. 31, no. 5, pp. 3945–3957, May 2016.
- [9] C. N.-M. Ho, V. S. P. Cheung, and H. S.-H. Chung, "Constant-frequency hysteresis current control of grid-connected VSI without bandwidth control," *IEEE Trans. Power Electron.*, vol. 24, no. 11, pp. 2484–2495, Nov. 2009.
- [10] H. Komurcugil, S. Bayhan, and H. Abu-Rub, "Variable- and fixed-switching-frequency-based HCC methods for grid-connected VSI with active damping and zero steady-state error," *IEEE Trans. Ind. Electron.*, vol. 64, no. 9, pp. 7009–7018, Sep. 2017.
- [11] M. Kumar and R. Gupta, "Sampled-Time-Domain analysis of a digitally implemented current controlled inverter," *IEEE Trans. Ind. Electron.*, vol. 64, no. 1, pp. 217–227, Jan. 2017.
- [12] F. Wu, F. Feng, L. Luo, J. Duan, and L. Sun, "Sampling period online adjusting-based hysteresis current control without band with constant switching frequency," *IEEE Trans. Ind. Electron.*, vol. 62, no. 1, pp. 270–277, Jan. 2015.
- [13] H. Mao, X. Yang, Z. Chen, and Z. Wang, "A hysteresis current controller for single-phase three-level voltage source inverters," *IEEE Trans. Power Electron.*, vol. 27, no. 7, pp. 3330–3339, Jul. 2012.
- [14] F. Wu, B. Sun, K. Zhao, and L. Sun, "Analysis and solution of current zero-crossing distortion with unipolar hysteresis current control in grid-connected inverter," *IEEE Trans. Ind. Electron.*, vol. 60, no. 10, pp. 4450–4457, Oct. 2013.
- [15] F. Wu, X. Li, and J. Duan, "Improved elimination scheme of current zero-crossing distortion in unipolar hysteresis current controlled grid-connected inverter," *IEEE Trans. Ind. Informat.*, vol. 11, no. 5, pp. 1111–1118, Oct. 2015.
- [16] J. K. Singh and R. K. Behera, "An improved hysteresis current controller for grid-connected inverter system to address power quality issues at reduced switching frequency," *IEEE Trans. Ind. Appl.*, vol. 57, no. 2, pp. 1892–1901, Mar. 2021.
- [17] G. H. Bode and D. G. Holmes, "Implementation of three level hysteresis current control for a single phase voltage source inverter," in *Proc. IEEE 31st Annu. Power Electron. Specialists Conf.*, vol. 1, Jun. 2000, pp. 33–38.
- [18] X. Li, Y. Liu, and H. Zhang, "Hybrid-modulation hysteresis scheme based decoupled power control of grid-connected inverter," *IEEE J. Emerg. Sel. Topics Power Electron.*, vol. 11, no. 1, pp. 276–287, Feb. 2023.
- [19] S. Jena, N. Tiwary, C. K. Panigrahi, and P. K. Sahu, "Performance improvement of grid integrated voltage source inverter using different hysteresis current controllers," in *Proc. IEEE 7th Uttar Pradesh Sect. Int. Conf. Electr. Electron. Comput. Eng. (UPCON)*, Nov. 2020, pp. 1–6.
- [20] J. K. Singh and R. K. Behera, "A comparative study on HCC method for grid-connected LCL filter with active damping," in *Proc. 21st Eur. Conf. Power Electron. Appl.*, 2019, pp. 1–10.
- [21] Y. Hu, Y. Deng, Q. Liu, and X. He, "Asymmetry three-level grid-connected current hysteresis control with varying bus voltage and virtual oversample method," *IEEE Trans. Power Electron.*, vol. 29, no. 6, pp. 3214–3222, Jun. 2014.
- [22] F. Bagheri, H. Komurcugil, O. Kukrer, N. Guler, and S. Bayhan, "Multi-input multi-output-based sliding-mode controller for single-phase quasi-Z-source inverters," *IEEE Trans. Ind. Electron.*, vol. 67, no. 8, pp. 6439–6449, Aug. 2020.
- [23] Y. He, H. S. Chung, C. N. Ho, and W. Wu, "Use of boundary control with second-order switching surface to reduce the system order for dead-beat controller in grid-connected inverter," *IEEE Trans. Power Electron.*, vol. 31, no. 3, pp. 2638–2653, Mar. 2016.
- [24] Y. Liu, B. Ge, H. Abu-Rub, H. Sun, F. Z. Peng, and Y. Xue, "Model predictive direct power control for active power decoupled single-phase quasi-Z-source inverter," *IEEE Trans. Ind. Informat.*, vol. 12, no. 4, pp. 1550–1559, Aug. 2016.
- [25] M. Pokharel, N. Hildebrandt, C. N. M. Ho, and Y. He, "A fast-dynamic unipolar switching control scheme for single-phase inverters in DC microgrids," *IEEE Trans. Power Electron.*, vol. 34, no. 1, pp. 916–927, Jan. 2019.
- [26] F. Peng, G. Zhou, N. Xu, and S. Gao, "Zero leakage current single-phase quasi-single-stage transformerless PV inverter with unipolar SPWM," *IEEE Trans. Power Electron.*, vol. 37, no. 11, pp. 13755–13766, Nov. 2022.
- [27] L. A. Serpa, S. D. Round, and J. W. Kolar, "A virtual-flux decoupling hysteresis current controller for mains connected inverter systems," *IEEE Trans. Power Electron.*, vol. 22, no. 5, pp. 1766–1777, Sep. 2007.
- [28] Y. He and Y. Wu, "A universal multicarrier multisampling method for digitally controlled inverters," *IEEE Trans. Power Electron.*, vol. 38, no. 1, pp. 385–395, Jan. 2023.



RUI XIE received the Ph.D. degree from the College of Electrical Engineering, Zhejiang University, Hangzhou, China, in 2010.

He is currently an Academic Leader of the Far-Shore Wind Power Transmission Laboratory, PowerChina Huadong Engineering Corporation Ltd., Hangzhou. His current research interests include HVAC/HVDC power system study and HVDC converter station design.



BIN LIN received the M.S. degree in electrical engineering from Zhejiang University, Hangzhou, China, in 2015.

He is currently an Engineer with PowerChina Huadong Engineering Corporation Ltd., Hangzhou. His current research interests include flexible HVDC transmission systems and wind turbine control strategies.



QINGFA ZENG received the M.S. degree in electrical engineering from Hangzhou Dianzi University, Hangzhou, China, in 2023.

His research interests include dc-ac power converters and renewable energy generation systems.



OUYANG XU received the M.E. degree from the College of Electrical Engineering, China Agricultural University, Beijing, China, in 2018.

He is currently an Electrical Professional Supervisor with PowerChina Huadong Engineering Corporation Ltd., Hangzhou, China. His current research interest includes designing offshore HVAC/HVDC wind farm.



FEI YANG received the M.S. degree in electrical engineering from Chongqing University, Chongqing, China, in 2010.

He is currently a Senior Engineer with PowerChina Huadong Engineering Corporation Ltd., Hangzhou, China. His current research interests include relay protection and control of offshore HVAC/HVDC wind farm.



YUANBIN HE (Member, IEEE) received the Ph.D. degree in electrical engineering from the City University of Hong Kong, Hong Kong, in 2017. From April 2013 to August 2013, he was a Research Assistant with the City University of Hong Kong, where he was a Postdoctoral Research Fellow, from February 2017 to July 2017. From February to June 2016, he was a Visiting Scholar with the University of Manitoba, Winnipeg, Canada. Since May 2017, he has been

with Hangzhou Dianzi University, Hangzhou, China, where he is currently an Associate Professor with the Department of Electrical Engineering and Automation. His current research interests include renewable energy generation systems, power quality, and smart grids.

...